Photodissociation of $ClONO_2$ at 235 nm: Final Product Yields and Energy Partitioning

Peng Zou, Jiho Park, Bridget A. Schmitz, Trieu Nguyen, and Simon W. North*

Department of Chemistry, Texas A&M University, College Station, Texas 77842

Received: August 8, 2001; In Final Form: October 10, 2001

The photodissociation of $ClONO_2$ at 235 nm was investigated using resonance enhanced multiphoton ionization time-of-flight mass spectrometry, which permits the state selective detection of $Cl(^3P_{3/2})$ (Cl) and $Cl(^3P_{1/2})$ (Cl*) atom products. The angular and speed distributions for the Cl, Cl*, and ClO channels were derived from forward convolution fitting of time-of-flight spectra. The anisotropy parameters for the Cl elimination channels are 0.5 ± 0.15 and 1.2 ± 0.15 for the atomic ground and excited states respectively, indicating that the states arise from different electronic excited states. The anisotropy parameter for the $ClO + NO_2$ channel is 1.0 ± 0.15. On the basis of simulations to the TOF data, we have determined a total Cl atom quantum yield of 0.42 ± 0.1 and a ClO quantum yield of 0.58 ± 0.1. The fraction of nascent NO_3 fragments that undergo secondary dissociation was calculated based on the measured internal energy distribution. The $NO_2 + O$ channel has a quantum yield of 0.20, and $NO + O_2$ channel has a quantum yield of 0.006. The results are discussed in light of previous measurements at both longer and shorter wavelengths and suggest that at short wavelengths the spontaneous secondary dissociation of NO_3 to yield $NO_2 + O$ is important and will substantially reduce the impact of the $Cl + NO_3$ channel on stratospheric ozone depletion.

I. Introduction

Halogenated compounds play a key role in atmospheric chemistry. The impact of chlorine species, in particular, on stratosphere ozone depletion has been well established.[1] Chlorine nitrate is one of most important temporary reservoir species of reactive chlorine.[2,3] A detailed understanding of $ClONO_2$ chemistry is critical for modeling global and seasonal ozone distributions in the stratosphere. The formation of $ClONO_2$ occurs primarily through the recombination reaction of ClO and NO_2

$$ClO + NO_2 + M \rightarrow ClONO_2 + M \quad (1)$$

and therefore couples the ClO_x and NO_x cycles.[4] The removal of chlorine nitrate and conversion to active chlorine results from either heterogeneous reactions or through day-time photolysis. Photolysis is predicted to be the dominant loss mechanism, except during the polar winter.[5] Several photochemical channels are energetically accessible in the stratosphere

$$ClONO_2 \xrightarrow{h\nu} ClO + NO_2 \quad (2)$$

$$ClONO_2 \xrightarrow{h\nu} Cl + NO_3 \quad (3)$$

$$ClONO_2 \xrightarrow{h\nu} ClONO + O \quad (4)$$

The energetics associated with each of these primary asymptotic channels are shown in Figure 1. Also included in the figure are the dissociation pathways for NO_3 radicals produced via channel 3. The relative branching ratios for these dissociation channels is important in evaluating the role of $ClONO_2$ in stratosphere ozone depletion. It is not surprising, therefore, that numerous experimental studies have been carried out to understand the photodissociation dynamics and kinetics of $ClONO_2$, especially the wavelength- and temperature-dependent branching ratios.[6]

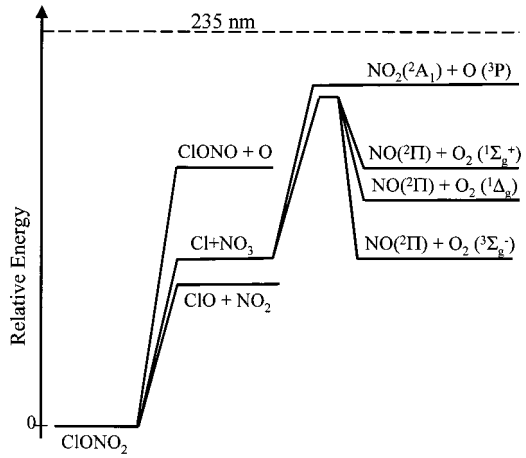

Figure 1. Schematic energy level diagram for $ClONO_2$ photodissociation. The secondary dissociation channels for NO_3 are also shown.

Although the $ClO-NO_2$ bond is the weakest in $ClONO_2$,[6] initial experimental studies reported that the $ClO + NO_2$ channel was only of minor importance. Knauth and Schindler reported that channel (3) was the dominant dissociation channel at 265 and 313 nm in a static cell.[7] Margitan observed that Cl and O atoms were the two major products with quantum yields of 0.9 and 0.1 respectively at 266 and 355 nm using the atomic resonance fluorescence detection method.[8] Low pressure ($<10^{-3}$ Torr) photolysis experiments were performed by Chang et al., and a quantum yield of 1.0 ± 0.2 for Cl atom was reported.[9] Subsequently, Burrows et al. studied the photolysis at 254 nm, and observed that the quantum yield of O atom was 0.24 and the quantum yield of NO_3 was 1.04.[10] Broadband photolysis

* To whom correspondence should be addressed. E-mail: north@mail.chem.tamu.edu.

10.1021/jp013099k CCC: $22.00
Published on Web 01/19/2002

by Nickolaisen et al. found that at $\lambda > 200$ nm, the relative quantum yields, assuming negligible contributions from other channels, are 0.61 ± 0.20 for Cl and 0.39 ± 0.20 for O; in the $\lambda > 300$ nm region, the quantum yields are found to be 0.44 ± 0.08 for Cl and 0.56 ± 0.08 for O atoms.[11] Marinelli and Johnston reported a nonunity NO_3 quantum yield of 0.55 ($+0.3/-0.1$) at 249 nm by direct absorption measurements of NO_3 at 662 nm.[12]

The first direct observation ClO products was made by Minton et al. employing molecular beam photofragment translational spectroscopy at 248 and 193 nm.[13] Subsequent experiments by their group revealed a wavelength-dependent Cl and ClO branching ratio and the absence of evidence for channel 4.[14,15] The authors also observed the secondary photodissociation of ClO radicals

$$ClO \xrightarrow{h\nu} Cl(^2P_{3/2}, ^2P_{1/2}) + O(^3P_J, ^1D_2) \qquad (5)$$

and suggested that the secondary dissociation of products ClO and NO_3 account for the O atoms observed in previous studies. Subsequent cell experiments also confirmed the importance of $ClO + NO_2$ channel. Quantum yields for channels 2 and 3 varied from 0.36 ± 0.08 and 0.64 ± 0.08 at 193 nm to 0.46 ± 0.08 and 0.54 ± 0.8 at 248 nm. Additional studies at 308 nm gave quantum yields of 0.33 ± 0.6 and 0.67 ± 0.6 for channels 2 and 3, respectively. Tyndall et al. observed quantum yields of 0.80 ± 0.20 and 0.28 ± 0.12 for Cl and ClO at 308 nm using resonance fluorescence detection methods, and a very small O (^3P) yield ≤ 0.05 was also reported.[16] Ravishankara and coworkers have studied the photodissociation of $ClONO_2$ at 193, 222, 248, and 308 nm using both atomic resonance fluorescence and time-resolved absorption methods. They found that Cl and ClO are the two major dissociation products at 222, 248, and 308 nm, whereas at 193 nm, the quantum yield of O became larger than the yield of ClO. The authors also suggested that NO_3 decomposition is one of the major sources of O atoms observed, which is consistent with a O quantum yield increase with decreasing of photolysis wavelength, but no quantitative model was proposed.

The product branching ratios in the photolysis of $ClONO_2$ are wavelength-dependent suggesting that several excited states may play a role in the dissociation dynamics. Ab initio calculations of singlet and triplet excited states by Graña et al. show that there are six singlet excited states with vertical excitation energies between 180 and 300 nm.[17] The wavelength-dependent branching ratios are likely the result of both the complex nature of the absorption spectrum and the excited state dynamics. To fully understand the contribution of the various excited states and obtain a predictive model of the photodissociation, experiments over a wide wavelength range are necessary. To quantify the primary product yields, secondary reactions, which may occur in static or flow cell experiments, need to be minimized and are likely the major reasons for early conflicting results. Photodissociation in a molecular beam provides a rarified environment in which to study the primary photochemistry in the absence of secondary collisions.

We have investigated the photodissociation of $ClONO_2$ at 235 nm using molecular beam techniques and time-of-flight mass spectroscopy (TOFMS) with resonance enhanced multiphoton ionization (REMPI) detection. The branching ratio of primary chlorine atoms and chlorine oxide was calculated from forward convolution (FC) fitting of TOFMS spectra. The fraction of NO_3 photofragments that undergo secondary dissociation, and the resultant decomposition channel branching ratio was determined according to the derived internal energy distribution. Finally, on the basis of the Cl quantum yield and the NO_3 internal energy distribution, a model was developed to predict the wavelength-dependent O atom quantum yield arising from spontaneous NO_3 secondary dissociation.

II. Experimental Section

A detailed description of the experimental setup can be found elsewhere.[18] Briefly, a differentially pumped molecular beam apparatus was used. A pulsed molecular beam of ~1% either chlorine nitrate or chlorine monoxide in helium was collimated by a conical skimmer and intersected by the laser pulses. The resulting ions were detected using a two-stage Wiley−McLaren time-of-flight mass spectrometer (TOF-MS) in 'core-sampled' mode.[19,20,21,22] A copper plate with a 3.0 mm pinhole was placed approximately 29 cm from the interaction region, allowing only a 'core' of the ion packet to strike the detector. The ions were detected by a set of dual Chevron microchannel plates located 51 cm from the interaction region. The core sampled signal was averaged a multichannel scaler with a 5 ns bin size.

A pulsed extraction electric field was utilized in order to increase the velocity resolution and signal intensity. The ion cloud is allowed to expand under field-free conditions for a period of time before the extraction field is applied to direct the ions toward the detector. Delay times between laser shots and extraction field are typically 500−800 ns. The arrival time of each ion is determined by the delay time and the projection of the initial velocity along the flight axis. Therefore, a large extraction-field strength can be applied for better velocity resolution. Compared to a continuous extraction field, there are two obvious advantages of pulsed field extraction. First, small variations in electrode voltages only have minor effects on the TOFMS spectra. Second, large field strengths in the first extraction stage limit the ion packet expanding in the plane perpendicular to flight axis, therefore increasing signal intensity. The rising-edge of the pulsed field is less than 25 ns, which guaranties that blurring is negligible.

The chlorine atoms were probed using 2 +1 REMPI transitions at 235.25 nm for spin−orbit ground-state Cl ($^2P_{3/2}$) and 235.13 nm for excited-state Cl ($^2P_{1/2}$) (hereafter referred to as Cl and Cl*, respectively).[23] The dye laser was pumped by 355 nm light from the third harmonic of a Nd:YAG laser operating at 10 Hz. The output of the dye laser was doubled in BBO and separated from the fundamental using two Pellin-Broca prisms. The polarization of the doubled light was rotated using a double Fresnel rhomb and a polarizer ensured >99% polarization of the light entering the chamber. The light was focused into the interaction region with a 300 mm lens, resulting in spot sizes between 50 and 300 μm. The laser power was typically 100−250 μJ/pulse.

Cl_2O was synthesized by the method of Cady.[24] Cl_2 was collected on prebaked HgO (Aldrich) powder and the reaction was allow to run overnight at 195 K. $ClONO_2$ was prepared by the method of Schmeisser through the reaction of N_2O_5 and Cl_2O.[25] The impurities in both Cl_2O and $ClONO_2$ (mainly Cl_2) were removed by vacuum distillation. The purity of samples was confirmed by UV−vis absorption spectroscopy. Though a small Cl_2 contamination always exists (<5%), it is difficult to completely remove without losing significant amount of sample. However, because the absorption cross section of Cl_2 is nearly 2 orders of magnitude smaller than that of Cl_2O and $ClONO_2$, the contribution of Cl_2 photolysis to the TOFMS spectrum should be negligible. In addition, the TOFMS spectrum of Cl atoms from the photodissociation of Cl_2 should produce sharp

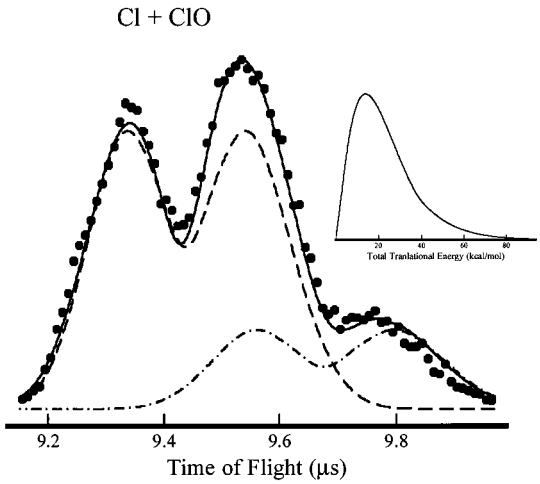

Figure 2. Cl TOFMS from Cl_2O photodissociation at 235 nm. Filled circles represent experimental data, the solid line is the FC fitting, the dashed line represents the contribution from ^{35}Cl isotope, and dashed−dot line represents contribution from ^{37}Cl isotope. The inset plot shows the translational energy distribution for Cl channel.

peaks corresponding to narrow speed distributions, which should be easily distinguished from the signal derived from Cl_2O and $ClONO_2$.

III. Results and Analysis

The forward convolution fitting procedure (FC) for core-sampled time-of-flight mass spectra has been described previously.[18] The photofragment velocity distribution, projected along the flight axis, is given by[26,27]

$$f(v_z,\chi) = \int_{|v_z|}^{\infty} \frac{g(v)}{2v}\left[1 + \beta P_2(\cos\chi) P_2\left(\frac{v_z}{v}\right)\right] dv \qquad (6)$$

where β is the spatial anisotropy parameter, $P_2(x)$ is the second Legendre polynomial, v_z is the projection of the fragment velocity on the detector axis, $g(v)$ is the center-of-mass speed distribution, and χ is the angle between the laser electric field vector and the flight axis, $\hat{z}$. In our one-color experiments, a linear polarized laser was used for both dissociation and REMPI detection. In FC fitting, $g(v)$ and β are iteratively adjusted to provide the best fit to the TOF data at different polarizations. 'Core-sampling' discriminates against ions with large velocity components perpendicular to the flight axis, and only those which satisfy the equation, $v_{xy} \leq r_{core}/t$, where v_{xy} is the projection of velocity on the plane perpendicular to the flight axis, r_{core} is the radii of the core, t is time-of-flight when ions reach the core, are detected.

A. Cl_2O Photodissociation at 235 nm. To ascertain the contribution of Cl_2O photolysis to the $ClONO_2$ data and calibrate our Cl/Cl* detection sensitivity, we have studied Cl_2O photodissociation at 235 nm. The photodissociation of Cl_2O has been investigated previously at 308, 248, and 193 nm using photofragment translational energy spectroscopy.[28] Recently, Tanaka et al. have studied the photodissociation of Cl_2O at 235 nm using REMPI photofragment ion imaging methods.[29] Figure 2 shows the TOFMS spectra of ground-state Cl from the photodissociation of Cl_2O at 235 nm with $\chi = 0°$. The filled circles represent the experimental data and the solid lines represent FC fitting. The inset shows the total translational energy distribution derived from the FC fitting of this channel. The resultant translational energy distributions of both Cl and Cl* channels (Cl* results are not shown here) and the measured anisotropy parameters

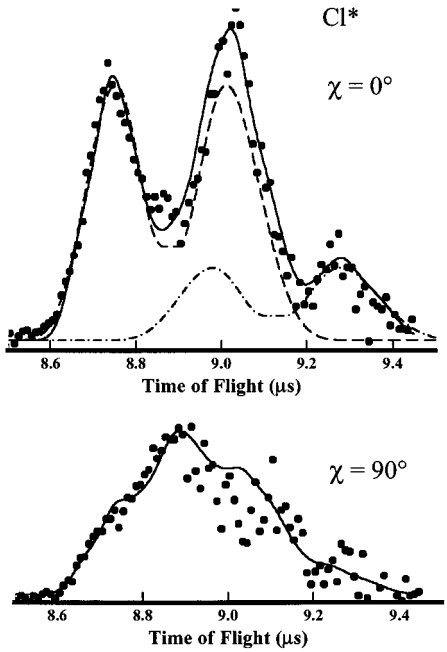

Figure 3. Cl* TOFMS from $ClONO_2$ photodissociation. Filled circles represent experimental data, the solid line is the FC fitting, dashed line represents the contribution from the ^{35}Cl isotope, and the dashed−dot line represents contribution from the ^{37}Cl isotope.

are in good agreement with the results of Tanaka et al.[29] To obtain the Cl/Cl* branching ratio, we scanned the laser over the Cl/Cl* Doppler profiles using equal laser power. The ratio of the integrated areas of the Cl and Cl* REMPI signals was corrected by the detection efficiency of Cl and Cl*

$$\mathrm{Cl/Cl^*} = \frac{I_{Cl}}{I_{Cl^*}} \times \frac{f_{Cl^*}}{f_{Cl}} \qquad (7)$$

where I_i are the integrated areas of the REMPI scans, and f_i are the relative detection sensitivities. The Cl/Cl* ratio obtained in this way is 0.062, very close to the value reported by Tanaka et al.[29]

B. $ClONO_2$ Photodissociation at 235 nm. Figure 3 shows the Cl* TOFMS spectra of $ClONO_2$ photodissociation at 235 nm taken at $\chi = 0°$ and $\chi = 90°$ experimental geometries, and Figure 4 shows the Cl TOFMS spectra. Both TOFMS spectra are substantially different from the Cl_2O spectra, which indicates that there is negligible Cl_2O contribution in the $ClONO_2$ spectra. The Cl* TOF profile consists of a single feature at large velocities and exhibits a strong positive anisotropy. Therefore, we attribute the Cl* products to primary Cl−O bond fission. The dashed and dot−dashed lines in the upper panel of Figure 3 correspond to contributions from the ^{35}Cl and ^{37}Cl isotopes, respectively. The $P(E_T)$ distribution for the primary Cl* channel is shown in Figure 5.

We find that the Cl TOFMS profiles from $ClONO_2$ photodissociation cannot be adequately fit with a single contribution. Analysis of the polarization dependence of the TOF profiles indicates that there are at least two contributions. To fit the TOF data, two contributions with positive anisotropy were used as illustrated by the $P(E_T)$ distributions in Figure 6. We attribute the fast feature (solid line) to primary Cl−O bond fission to give ground-state Cl. The slow feature (dashed line) arises from the secondary photodissociation of ClO photofragments.

Nelson et al. have observed the secondary photodissociation of ClO previously.[15] Because the Cl atom product from secondary dissociation will bias the relative branching ratio of

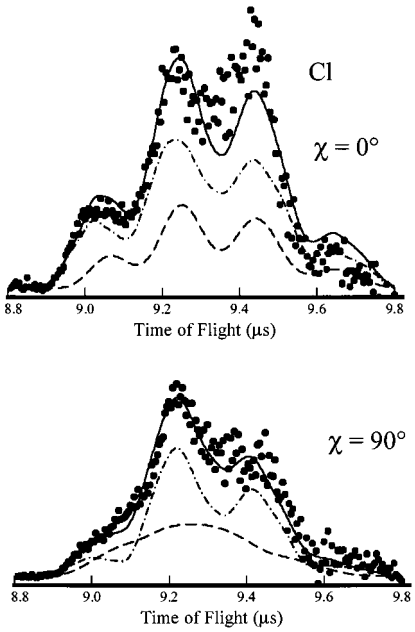

Figure 4. Cl TOFMS from $ClONO_2$ photodissociation. Filled circles represent experimental data, the solid line is the FC fitting result, the dashed line represents the Cl component from ClO secondary dissociation, and dashed−dot line represents the Cl component from primary $ClONO_2$ dissociation.

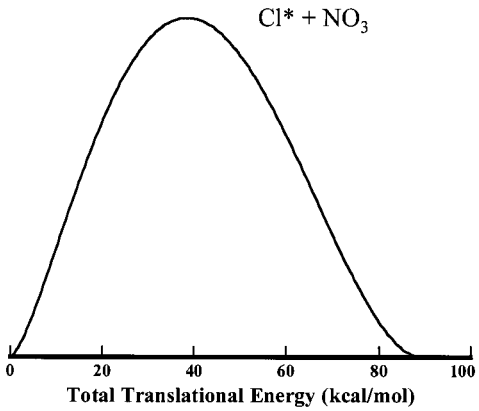

Figure 5. Translational energy distribution for Cl* dissociation channels for $ClONO_2$ photodissociation at 235 nm.

the Cl and ClO channels, the laser power was decreased in their experiment to minimize the effect of secondary photodissociation of ClO. Despite lowering the laser power, secondary photodissociation of ClO is unavoidable because of the similar absorption cross sections of ClO and $ClONO_2$ for the wavelength region under investigation. Under our experimental conditions with the very tightly focused beam required for 2 + 1 REMPI detection, we estimate that all the ClO products undergo photodissociation. Although this process could be viewed as a limitation, it is actually quite beneficial since saturation of the ClO secondary photodissociation provides the means to determine the branching ratio of channels (2) and (3) by measuring only the Cl atom TOFMS spectra. Of course, the analysis requires that on the basis of FC simulations, one can distinguish the signal arising from primary Cl and Cl from the ClO photodissociation. The FC fitting procedure required modification in order to account for secondary ClO photodissociation and to derive the angular and speed distributions of primary Cl and ClO photofragments.

The contribution to the Cl TOFMS spectra arising from secondary ClO photodissociation is a convolution of the ClO

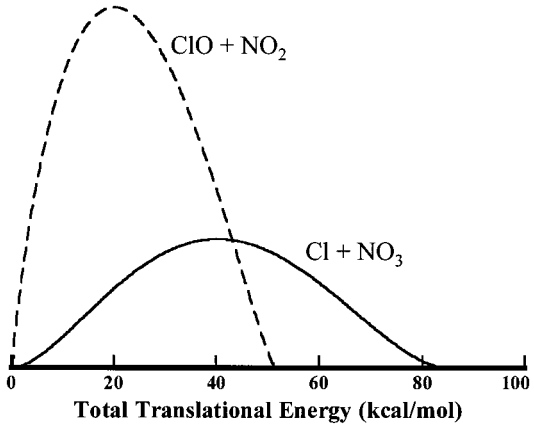

Figure 6. Translational energy distributions for the ClO and Cl dissociation channels for $ClONO_2$ photodissociation. The dashed line represents the ClO + NO_2 $P(E_T)$ distribution and the solid line represents Cl + NO_3 $P(E_T)$ distribution.

velocity distribution from primary $ClONO_2$ photodissociation with Cl velocity distribution from the secondary ClO photodissociation (8)

$$I(v_z;\chi) = \int_{v_{xy} \le r_{core}/t} I_{ClO}(v_{zClO};\chi) I_{Cl}(v_{zCl};\chi) dv \qquad (8)$$

where v_{zClO} is the *z*-axis component of velocity of ClO from primary $ClONO_2$ dissociation, v_{zCl} is the *z*-axis component of velocity of Cl from secondary ClO dissociation, v_z is the vector sum of v_{zClO} and v_{zCl}, $I_{ClO}(v_{zClO};\chi)$ is the velocity distribution of ClO from $ClONO_2$ photodissociation, $I_{Cl}(v_{zCl};\chi)$ is the velocity distribution of Cl from secondary ClO photodissociation. The resultant velocity is a vector sum of velocities obtained at the primary dissociation and secondary dissociation, $\vec{v} = \vec{v}_{ClO} + \vec{v}_{Cl}$, and the evaluation is required for every possible $\vec{v}_{ClO}$ and $\vec{v}_{Cl}$ combination.

To correctly account for $I_{Cl}(v_{zCl};\chi)$, we carried out experimental studies of ClO photodissociation at 235 nm using the same apparatus with a pulsed discharge radical source.[30] Among the four allowed asymptotic electronic channels, the dominant products (> 97%) are $Cl(^2P_{3/2}) + O(^1D_2)$ with an anisotropy parameter of 1.2 ± 0.2. The $Cl(^2P_{1/2}) + O(^3P_J)$ channel constitutes < 2% at this wavelength. The results are very similar to the work of Davis and Lee at 248 nm using photofragment translational energy spectroscopy.[31] The translational energy arising from ClO dissociation can be precisely calculated with the known dissociation threshold, the internal energy of parent molecule, and the spin−orbit splitting of atomic products, assuming that the electronic branching is not strongly dependent on the parent initial state. The soft fragment impulsive model[32] was used to estimate the ClO internal energy in the FC simulations. Because $I_{Cl}(v_{zCl};\chi)$ is known, the $P(E_T)$ distribution of ClO can be iteratively determined by FC fitting of the experimental TOFMS spectra. The weighted $P(E_T)$ distribution for primary Cl and ClO can then be used to calculate the branching ratio between these two channels. The total Cl/Cl* branching ratio was determined by integrating REMPI scans for Cl and Cl* and then correcting the signals using the Cl and Cl* detection efficiencies, as in Cl_2O photodissociation.[23,33]

Figure 6 shows the total translational energy distribution for the Cl and ClO channels derived from the FC fitting procedure described above. The translational energy distributions for primary Cl and Cl* products are almost identical except that the Cl distribution is slightly more energetic than the Cl* distribution. Similar average translation energies of Cl and Cl*

TABLE 1: Anisotropy Parameters and Average Translational Energy for the Cl + NO_3, Cl* + NO_3, and ClO + NO_2 Channels

	193 nm [b]		235 nm				248 nm [b]	
	β	$\langle E_T\rangle^a$	β	β_{avg}	$\langle E_T\rangle^a$	$\langle E_T\rangle_{avg}$	β	$\langle E_T\rangle^a$
Cl+NO_3	0.5 ± 0.15	42.8	0.5 ± 0.15	0.74	41.3	41.1	0.5 ± 0.15	40.6
Cl*+NO_3			1.2 ± 0.15		40.7			
ClO+NO_2	0.25 ± 0.15	22.9	1.0 ± 0.15		23.0		1.15 ± 0.15	22.5

[a] In kcal/mol. [b] Reference 15.

TABLE 2: Quantum Yields of Cl, ClO, and O from $ClONO_2$ Photodissociation at 235 nm

	193 nm	235 nm	248 nm
Cl	0.64 ± 0.08[a] 0.5[b]	0.42 ± 0.10	0.54 ± 0.08[a] 0.6[b]
ClO	0.36 ± 0.08[a] 0.3[b]	0.58 ± 0.10	0.46 ± 0.08[a] 0.4[b]
O	0.4[b]	0.20[c]	<0.10[b]

[a] Reference 15. [b] Recommended values from ref 6. [c] Calculated from the internal energy distribution of NO_3 and the thermodynamic threshold for the NO_2 + O channel.

products in the photodissociation is not uncommon for moderate sized molecules because the asymptotic channels have similar available energies due to the small spin−orbit splitting (2.5 kcal/mol).[34] The contributions to the Cl TOF spectra (Figure 4) arising from from primary dissociation of $ClONO_2$ and secondary dissociation of ClO are represented by the dashed lines and dash−dot lines, respectively. Because the major Cl products from ClO photodissociation are in their ground state, contribution from secondary ClO dissociation can only be observed in the TOFMS spectra of Cl.

IV. Discussion

A. Fragment Angular and Speed Distributions. The anisotropy parameters and average total translational energies for the different dissociation channels are given in Tables 1 and 2 together with the results from Nelson et al. at 193 and 248 nm.[28] The angular distributions of products can provide valuable information on the nature of the excited states involved in the photodissociation. The anisotropy parameter depends on the excited-state lifetime, the orientation of transition dipole moment with respect to the recoil axis, and geometry changes in the course of dissociation. All the dissociation channels at 235 nm show measurable positive anisotropy parameters, indicating that the lifetime of the excited states must be much shorter than the rotational period of the parent molecule (<1ps).[35]

The ground-state equilibrium geometry of $ClONO_2$ is planar with C_s symmetry.[17] The positive anisotropy parameters indicate that parallel transitions, involving excited states with A' symmetry, are involved in the dissociation because the transition dipole moment of excitation to A' states lies in the molecular plane.[28] The A'' states cannot be excluded completely from the current experimental results, because the contribution from a A'' state will decrease the anisotropy, and this effect depends on the magnitude of the contribution.

Because the current experiments represent the first state-selected measurements of Cl and Cl* from $ClONO_2$ photodissociation, the average values of total translational energy and anisotropy parameter were calculated in order to facilitate comparison of our results with the state-averaged measurements of Nelson et al. This was done by weighting the distributions and anisotropy parameters for the Cl and Cl* channels using the primary Cl*/Cl ratio of 0.52 determined from FC fitting. The results are shown in Table 1. The average anisotropy parameter for the Cl + NO_3 channel is slightly higher than the values at 193 and 248 nm. The translational energy, however, does not change significantly with the decrease of available energy by 32.9 kcal/mol from 193 to 248 nm, which is inconsistent with a simple model of energy partitioning for dissociation on a single repulsive excited state. This suggests that different excited states may contribute to this channel throughout the absorption spectrum. In addition, the anisotropy of the Cl* channel is substantially different from the Cl channel. Very likely, these two channels originate from different excited states at 235 nm. The anisotropy of the ClO channel changes from 0.25 ± 0.15 to 1.15 ± 0.15 from 193 to 248 nm. Our result at 235 nm is 1.0 ± 0.2, close to the value 248 nm, suggesting that the excited state(s) are the same at both 235 and 248 nm but different from 193 nm.

B. Final Product Branching Ratio. An important subject of the present studies is a determination of the branching ratio of the Cl/ClO channels. The total Cl atom quantum yield can be calculated using

$$\Phi^{Cl}_{total} = 1 - \frac{\Omega_{cl/cl^*} \times p_{clo/cl}}{(p_{clo/cl} \times \Omega_{cl/cl^*} + p_{clo/cl} + \Omega_{cl/cl^*} + 1)} \quad (9)$$

where Ω_{cl/cl^*} is the total Cl/Cl* ratio from REMPI scan (4.4) and $p_{clo/cl}$ is the ratio of primary ClO to Cl from FC fitting of the Cl TOFMS data. The absolute quantum yields of Cl* and ClO can be calculated similarly. To report absolute quantum yields, we have assumed that the total dissociation quantum yield is unity. The quantum yield results are presented in Table 2. Our results are in reasonable agreement with both molecular beam measurements of Nelsons et al.[15] and measurements of Ravishankara and co-workers within the mutual error bars. A comparison of our quantum yield results with the results of Ravishankara and co-workers reveal that our Cl quantum yield at 235 nm is slightly lower than their values at 193 and 248 nm, whereas the ClO quantum yield is higher. The quantum yield we report here is actually the total Cl atom quantum yield from primary dissociation of $ClONO_2$. In the studies of Ravishankara and co-workers, the authors are unable to distinguish between primary and secondary photodissociation and only the total Cl quantum yield can be measured. Contributions from ClO products secondary photodissociation would result in a decrease of ClO quantum yield and an increase in the Cl quantum yield. We have assumed in our analysis that channel (4), the primary elimination of oxygen atoms is negligible at 235 nm. The quantum yield of O atom is not zero, however, due to the secondary dissociation of hot NO_3, which will be discussed in detail in next section.

According to calculations of $ClONO_2$ excited states by Graña et al.,[17] six or more excited states may contribute to the absorption spectrum in this wavelength region including three states that have A' symmetry. The 4 A' state, which has a $\pi\rightarrow\pi^*$ character localized on the NO_2 chromophore with vertical excitation energy of 6.62 eV (188 nm), has a very strong oscillator strength, 0.1849, compared to 0.0126 for the 3 A' state and 0.006 for the 2 A' state. Although the small variation of the Cl and ClO quantum yield ratios at 248 and 193 nm could

suggest that the 4 A' state may dominate in the UV region the variance in the ClO channel anisotropy indicates that the situation is considerably more complicated.

C. Secondary Dissociation of NO_3. Nascent NO_3 fragments produced via channel (2) with sufficient internal energy can undergo spontaneous secondary dissociation. The importance of this secondary process depends on the competition between two dissociation channels

$$NO_3 \rightarrow NO + O_2 \tag{10}$$

$$NO_3 \rightarrow NO_2 + O \tag{11}$$

because the $NO + O_2$ channel leads to direct ozone depletion. It is important, therefore, to determine the branching ratio between these two channels.

A schematic energy level of NO_3 dissociation is shown in Figure 1. The thresholds for the $NO + O_2$ and $NO_2 + O$ channels differ by less than 1 kcal/mol. Near-threshold experiments show that at energies above the $NO_2 + O$ threshold, dissociation leads to this channel exclusively.[36,37] The $NO + O_2$ channel is only observed when the excitation energy lies within the narrow energy region between the two thresholds. This result is consistent with the 'loose' nature of the $NO_2 + O$ transition state, in contrast to the $NO + O_2$ tight transition state.

Davis et al. have measured the NO_3 decay rates between the < 1 kcal/mol interval above the $NO + O_2$ threshold using picosecond resolution measurements. The rate was found to vary from 1×10^9 s^{-1} to 5×10^9 s^{-1} and was fitted by an RRKM theory calculation with a 70 cm^{-1} transition state frequency.[38] Mikhaylichenko et al. also performed the measurement of decomposition rate of NO_3 near the $NO + O_2$ threshold regime using laser induced fluorescence methods. Their result varied from 1×10^4 s^{-1} at 16 780 cm^{-1} to 6×10^7 s^{-1} at 16 880 cm^{-1}.[37] We have performed variational RRKM calculation of NO_3 decay rate with internal energy above the $NO_2 + O$ threshold. The rate varies from 1×10^9 s^{-1} with 1 kcal/mol above the threshold to 4×10^{10} s^{-1} with 5 kcal/mol above the threshold. Our calculations indicate that only NO_3 radicals with internal energy close to the threshold may be collisionally stabilized in the lower stratosphere where the magnitude of collision frequency is $\sim 10^9$. The solar flux near 235 nm becomes significant only at altitudes above 30−35 km, where the gas density is considerably lower than in the lower stratosphere. Therefore, most of the nascent NO_3 radicals with energy above the $NO_2 + O$ threshold will undergo secondary dissociation before collisional stabilization.

If we assume a unit dissociation quantum yield for internal energies above threshold the results for the secondary NO_3 dissociation represent an *upper limit*. Figure 7 shows the internal energy distribution of the NO_3 radicals averaged over the Cl/Cl* branching ratio at 235 nm. The two straight lines represent the energy threshold for the $NO + O_2$ and $NO_2 + O$ channels as shown. A comparison of the three areas of the distribution in Figure 7 indicates that $NO + O_2$ secondary dissociation is a minor channel with a quantum yield of 0.006. The quantum yield for the $NO_2 + O$ channel is 0.20, which should account for the O atom yield at 235 nm.

D. Wavelength-Dependent O Atom Quantum Yield. The O atom quantum yield arising from NO_3 secondary dissociation depends on both the yield of the Cl/Cl* + NO_3 channel and the NO_3 radical internal energy distribution. Because the quantum yield of Cl/Cl* + NO_3 channel only varies slightly from 193 to 308 nm, we have used the average value though

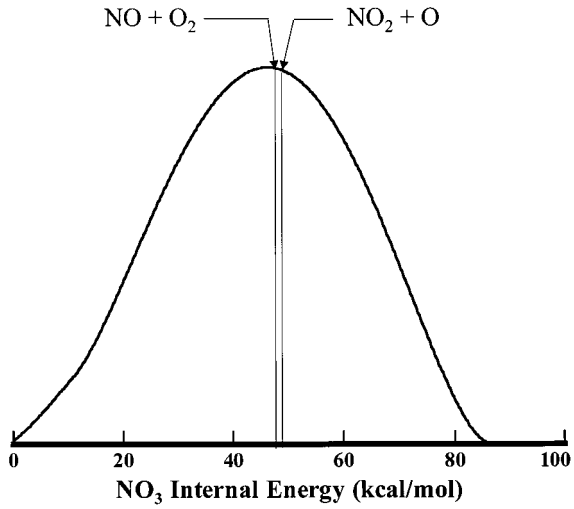

Figure 7. Internal energy distribution of NO_3 radicals, averaged over the Cl/Cl* branching ratio.

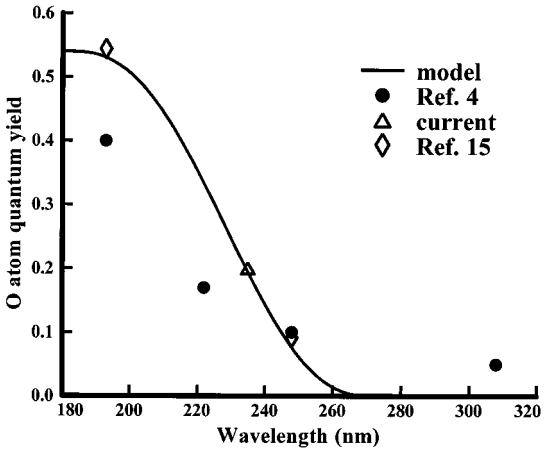

Figure 8. Wavelength-dependent O atom quantum yields. The solid line is based on the model described in the text.

the wavelength region of interest. The average total translational energy distribution of the Cl/Cl* + NO_3 channel has a linear dependence on the wavelength. A linear function was adopted to predict the average internal energy of NO_3 radicals

$$\langle E_{\text{int}}^{NO_3}(\lambda)\rangle = E_{h\nu} - D_0^0(\text{Cl} - \text{O}) - \langle E_T(\lambda)\rangle - E_{SO}^{Cl} \tag{12}$$

where $E_{h\nu}$ is the photon energy, D_0^0(Cl−O) is the bond dissociation energy, and E_{SO}^{Cl} is the Cl spin−orbit energy. A Gaussian function was adopted to represent the internal energy distribution of NO_3 with a fwhm linearly depending on the available energy.[39]

The modeling results for the wavelength-dependent O quantum yields from NO_3 secondary dissociation are shown in Figure 8. The solid line represents the model calculation, the filled circles represent the results of Ravishankara and co-workers, the triangle represents our result, and the diamonds represent the results of Nelson et al. At short wavelengths, the O atom quantum yields are determined solely by the quantum yield of Cl + NO_3 channel since all the NO_3 radicals have sufficient internal energy for secondary dissociation. At wavelengths $>$ 265 nm, no NO_3 radicals have sufficient internal energy for decomposition and the O atom quantum yield drops to zero. The model fits the results of Nelson et al. and current studies very well. Results from Ravishankara and co-workers at 308 and 248 nm were reported as upper limits. The O atom yields

at shorter wavelengths, 193 and 222 nm, are slightly lower than the model prediction. Results of Nelson et al. and the present work are based on the total translational energy distribution of $Cl + NO_3$ channel, and the experiments were carried out under molecular beam conditions. A fast-flow cell was used in Ravishankara and co-workers experiments with typical pressures of 40−100 Torr. To measure the total O atom quantum yield, N_2 gas was used to quench any possible $O(^1D_2)$ to $O(^3P_J)$ for detection. However, some of the nascent NO_3 from $ClONO_2$ was likely collisionally stabilized under these conditions, and this may be the major reason for the discrepancy with the model. The model has not considered the contribution from the O + ClONO channel although since the model fits the experimental results moderately well, this contribution may still be negligible for wavelengths as short as 193 nm.

The increase of three-body processes at short wavelengths will reduce the impact of the $Cl + NO_3$ channel on stratospheric ozone depletion. The photolysis of thermalized NO_3 produces $NO_2 + O$ and $NO + O_2$ in a 0.9/0.1 ratio based on the dominant absorption band of NO_3 near 660 nm.[40] The photolysis frequency of $ClONO_2$ at different altitudes can be readily calculated based on the actinic solar flux and $ClONO_2$ absorption cross section.[41] The results indicate that both UV and visible photodissociation of $ClONO_2$ are equally important except in the lower stratosphere (<20 km) where little UV light is available. A significant fraction of $ClONO_2$ photolysis at short wavelengths will produce hot NO_3 radicals that will undergo secondary dissociation. According to our model of NO_3 secondary dissociation, $NO + O_2$ is only a minor channel which means that NO_3 radicals arising from the $ClONO_2$ photolysis at wavelengths shorter than 260 nm will reduce the net $NO + O_2$ production relative to NO_3 photolysis. Assessment of the overall effect of the three-body dissociation of $ClONO_2$ must also include the decrease in $ClONO_2$ at higher altitudes due to a reduced termolecular formation rate.

V. Conclusions

We have examined the photodissociation of $ClONO_2$ and Cl_2O at 235 nm using TOFMS with 2 + 1 REMPI detection. A forward convolution fitting method was developed to incorporate the secondary photodissociation of ClO and model the primary photofragment angular and speed distributions. The absolute quantum yields for the Cl and ClO channels were measured to be 0.42 ± 0.1 and 0.58 ± 0.1, respectively. These branching ratio results are in good agreement with previous experimental studies at shorter and longer wavelengths. In addition, the role of secondary dissociation of NO_3 has been evaluated using the state-selected Cl/Cl* translational energy distributions. On the basis of the experimental results and previous studies, a model for the wavelength-dependent O atom quantum yield was developed. The results suggest that at short wavelengths (<260 nm) the spontaneous secondary dissociation of NO_3 is nonnegligible and will reduce the impact of the $Cl + NO_3$ channel. We anticipate that these studies can be extended to the longer wavelength tail of the absorption spectrum.

Acknowledgment. Work by B.A.S. was supported by National Science Foundation REU program. The authors thank W. Sean McGivern for valuable comments. Support for this project was provided by the Texas Research Endowment Program and a Research Enhancement Grant from Texas A&M University.

References and Notes

(1) Molina, M. J.; Molina, L. T. *ACS Symp. Ser*. **1992**, *483*, 24; Rowland, F. S. *Ing. Ambientale: Inquinamento Depurazione* **1977**, *6*, 317.

(2) Rowland, F. S.; Spencer, J. E.; Molina, M. J. *J. Phys. Chem*. **1976**, *80*, 2711.

(3) Rowland, F. S.; Spencer, J. E.; Molina, M. J. *J. Phys. Chem*. **1976**, *80*, 2713.

(4) Farman, J. C.; Gardiner, B. G.; Shanklin, J. D. *Nature*, **1985**, *315*, 207.

(5) Scientific Assessment of Ozone Depletion: 1994. Global Ozone Research and Monitoring Project. Technical Report No. 37; World Meteorological Organization: Geneva, 1994; Burkholder, J. B.; Talukdar, R. K.; Ravishankara, A. R. *Geophys. Res. Lett.* **1994**, *21*, 585.

(6) Goldfarb, L.; Schmoltner, A.-M.; Gilles, M. K.; Burkholder, J. B.; Ravishankara, A. R. *J. Phys. Chem. A*, **1997**, *101*, 6658−66; Yokeson, R. J.; Burkholder, J. B.; Fox, R. W.; Ravishankara, A. R. *J. Phys. Chem. A*, **1997**, 6667−6678; and references therein.

(7) Knauth, H. D.; Schindler, R. N. *Z. Naturforsch., A: Phys., Phys. Chem., Kosmophys*. **1983**, *38A*, 893.

(8) Margitan, James J. *J. Phys. Chem*. **1983**, *87*, 674.

(9) Chang, J. S.; Barker, J. R.; Davenport, J. E.; Golden, D. M. *Chem. Phys. Lett*. **1979**, *60*, 385.

(10) Burrows, J. P.; Tyndall, G. S.; Moortgat, G. K. *J. Phys. Chem*. **1988**, *92*, 4340.

(11) Nickolaisen, Scott L.; Sander, Stanley P.; Friedl, Randall R. *J. Phys. Chem*. **1996**, *100*, 10 165.

(12) Marinelli, W. J.; Johnston, H. S. *Chem. Phys. Lett*. **1982**, *93*, 127.

(13) Minton, T. K.; Nelson, Christine M.; Moore, T. A.; Okumura, M. *Science* **1992**, *258*, 1342.

(14) Moore, T. A.; Okumura, M.; Tagawa, M.; Minton, T. K. *Faraday Discuss.* **1995**, *100*, 295.

(15) Nelson, C. M.; Moore, T. A.; Okumura, M.; Minton, T. K. *Chem. Phys*. **1996**, *207*, 287.

(16) Tyndall, G. S.; Kegley-Owen, C. S.; Orlando, J. J.; Calvert, J. G. *J. Chem. Soc., Faraday Trans.* **1997**, *93*, 2675.

(17) Graña, A. M.; Lee, T. J.; Head-Gordon, M.*J. Phys. Chem*. **1995**, *99*, 3493.

(18) McGivern, W. S.; Li, R.; Zou P.; North S. W. *J. Chem. Phys*. **1999**, *110*, 5771.

(19) Wiley, W. C.; McLaren, I. H. *Rev. Sci. Instrum.* **1955**, *26*, 1150.

(20) Hwang, H. J.; Griffiths, J.; El-Sayed, M. A. *Int J. Mass Spectrom. Ion Processes* **1994**, *131*, 265.

(21) Ogorzalek-Loo, R.; Haerri, H.-P.; Hall, G. E.; Houston, P. L. *J. Chem. Phys.* **1989**, *90*, 4222.

(22) Syage, J. A. *J. Chem. Phys.* **1996**, *105*, 1007.

(23) Arepalli, S.; Presser, N.; Robie, D.; Gordon, R. J. *Chem. Phys. Lett.* **1985**, *118*, 88.

(24) Cady, G. H. *Inorg. Synth.* **1957**, *5*, 156.

(25) Schmeisser, M. *Inorg. Synth.* **1967**, *9*, 127.

(26) Zare, R. N. *Mol. Photochem.* **1972**, *4*, 1.

(27) Dixon, R. N. *J. Chem. Phys*. **1986**, *85*, 1866.

(28) Nelson, C. M.; Moore, T. A.; Okumura, M.; Minton, T. K. *J. Chem. Phys.* **1994**, *100*, 8055.

(29) Tanaka, Y.; Kwasaki, M.; Matsumi, Y.; Fujiwara, H.; Ishiwata, T.; Rogers, L. J.; Dixon, R. N.; Ashfold, N. R. *J. Chem. Phys.* **1998**, *109*, 1315.

(30) Zou, P.; Kim, H.; North, S. W *J. Chem. Phys*., in press **2001**.

(31) Davis, H. F.; Lee, Y. T. *J. Phys. Chem.* **1996**, *100*, 30.

(32) Busch, G. E.; Wilson, K. R. *J. Chem. Phys.* **1972**, *56*, 3639.

(33) The detection efficiency of the Cl ($^2P_{1/2}$) and Cl ($^2P_{3/2}$) transitions at 235.205 and 235.336 nm respectively have been well established by calibration to the spin−orbit measurements of HCl dissociation at 193 nm by Wittig and co-workers (Zhang, J.; M. Dulligan, M.; Wittig, C., *J. Chem. Phys.* **1997**, *107*, 1403). Using the results of ref 23, the previous published values for the relative Cl/Cl* line strengths of 0.8, has been adjusted to 0.6.

(34) Zou, P.; Mcgivern, W. S.; North, S. W. *Phys. Chem. Chem. Phys.* **2000**, *2*, 3785.

(35) Yang, S.; Bersohn, R. *J. Chem. Phys.* **1974**, *61*, 4400.

(36) Davis, H. F.; Kim, B.; Johnson, H. S.; Lee, Y. T. *J. Phys. Chem.* **1993**, *97*, 2172.

(37) Mikhaylichenko, K.; Riehn, C.; Valachovic, L.; Sanov, A.; Wittig, C. *J. Chem. Phys.* **1993**, *105*, 6807.

(38) Davis, H. F.; Ionov, P. I.; Ionov, S. I.; Wittig, C. *Chem. Phys. Lett.* **1993**, *215*, 214.

(39) The fwhm for the Guassian internal energy distribution are 25.7 kcal/mol at 193 nm and 18.9 kcal/mol at 248 nm.

(40) Brasseur, G. P.; Orlando, J. J.; Tyndall, G. S. *Atmospheric Chemistry and Global Change*; Oxford: New York, 1999.

(41) DeMore, W. B.; Sander, S. P.; Golden, D. M.; Hampson, R. F.; Kurylo, M. J.; Howard, C. J.; Ravishankara, A. R.; Kolb, C. E.; Molina, M. J. "Chemical Kinetics and Photochemical Data for use in Stratospheric Modeling"; *JPL Publ.* 92, NASA Jet Propulsion Lab., Pasadena, CA. **1992**.